Chapter 2

An atomic force microscopy study of the (001) surface of triclinic hen egg-white lysozyme crystals

The (001) surface of triclinic hen egg-white lysozyme-nitrate crystals has been investigated by *in-situ* atomic force microscopy to compare its growth mechanisms and properties to those of other lysozyme pseudo-polymorphs. The crystal morphology derived from connected net analysis using the macrobond concept is in good agreement with the experimental morphology of the crystals. Surface structures observed by AFM include rounded steps, growth spirals, 3D nucleation and impurity pinning. The growth spirals are rounded and highly anisotropic. Both screw and edge dislocations are found, characterised by hollow core outcrops. The observed hollow core radii are an order of magnitude larger than theoretical values, but do depend on supersaturation. From the rounded shape of the spirals and the absence of 2D nucleation we find an edge free energy $1.3 < \gamma_m/kT < 3$, which is similar to values found for tetragonal lysozyme. Serrated step patterns indicate impurity pinning. Complete blocking by impurities is not found. The step velocity is proportional to the relative

supersaturation. Using the kinetic coefficient, we find a sticking fraction of 4×10^{-4} for HEWL molecules to become attached to a kink, which is significantly higher compared to the sticking fraction for orthorhombic lysozyme.

2.1 Introduction

X-ray diffraction is the main route towards structure determination of protein macromolecules. To increase X-ray resolution scientists continue to search for methods to improve protein crystal quality, using both practical and fundamental approaches[1]. In both approaches hen egg-white lysozyme (HEWL) is often used as a model compound to test new techniques and ideas.

Lysozyme can be crystallised in various crystal structures, for example tetragonal, orthorhombic, monoclinic and triclinic[2, 3]. The crystal structure obtained depends on the choice of the salt used as crystallising agent. Using sodium nitrate as a crystallising agent, monoclinic as well as triclinic HEWL can be grown[4, 5]; sodium chloride yields tetragonal HEWL. In the tetragonal form, chloride ions are incorporated into the crystal structure, whereas in the triclinic form nitrate ions are incorporated. Therefore, these different lysozyme crystal structures are pseudo-polymorphs.

Atomic force microscopy (AFM) is often used to investigate crystallisation mechanisms, because crystal growth is a surface process. Most AFM studies on HEWL involve the tetragonal form[6, 7], despite that this crystal structure with eight molecules per unit cell is the most complex of all HEWL pseudo-polymorphs. Few AFM studies involve other pseudopolymorphs of lysozyme (orthorhombic[8], monoclinic[9]). Triclinic lysozyme has the most simple structure with only one molecule per unit cell. This implies a Kossel-like [10] growth mechanism for triclinic lysozyme, which should make the growth process relatively simple to understand. In spite of its simplicity and yielding the highest XRD resolution[11], the growth mechanisms of triclinic lysozyme have not yet been investigated in detail. In this paper we aim for a more quantitative understanding of the growth mechanisms and properties of triclinic lysozyme-nitrate crystals, such as morphology, spiral growth, step kinetics and the edge

free energy, and compare our observations with other pseudo-polymorphs to investigate similarities and differences.

2.2   Experimental procedures

2.2.1   Crystal growth

HEWL from Sigma-Aldrich (lot nrs. 51K7028 and 81K1554) was used, without further purification, as source material for crystal growth. Sodium nitrate, sodium acetate and acetic acid were all of analytical grade. A buffer stock solution of sodium acetate and acetic acid was made in deionised water (>15 MΩcm) to result in a 0.05 M NaCH$_3$COO/HCH$_3$COO solution of pH 4.5. Salt and lysozyme stock solutions were made in buffer solution. The buffer, salt and protein stock solutions were filtered over 0.2 μm membranes (Schleicher & Schuell). By mixing these three stock solutions, the crystallisation solutions were prepared containing 10 mg/ml HEWL and 0.2 M NaNO$_3$ in 0.05 M NaCH$_3$COO/HCH$_3$COO buffer.

A glass cell of 2 ml volume was filled with mother liquor. This glass cell was placed in a larger water flow cell. Temperature was controlled by flowing water from a Julabo F25 temperature controlled water bath around the glass cell. To grow triclinic lysozyme crystals, a strategy similar to that reported in [5] was used. First, the temperature is set at 4 $^{\circ}$C for 12 hours to induce nucleation. This turns the solution turbid and both monoclinic and triclinic crystals are formed. After 2 hours, the glass cell is taken out of its flow cell and subsequently left at room temperature (18-25°C) for 5 to 6 days. At room temperature the number of nuclei is largely reduced and the turbid system turns clear. The meta-stable monoclinic crystals dissolve, while the stable triclinic crystals continue to grow slowly.

2.2.2   *In-situ* atomic force microscopy

To prepare the triclinic lysozyme crystals for AFM measurements the contents of the glass cell is emptied into a glass petri-dish. A solution of 3 mg/ml HEWL

and 0.2 M NaNO$_3$ in sodium acetate buffer of pH 4.5 is added up to the rim of the petri-dish (12 ml in total). Then the petri-dish is sealed off, preventing exposure of the solution to the ambient air. Exposure to the ambient air results in the growth of spherulites and a surplus of small crystallites. The solution containing triclinic crystals is left at room temperature for a further 2 days. During this period of continued growth the crystals adhere to the glass bottom of the petri-dish, which prevents specimen slip during the AFM measurements

Before measurements a part of the solution is removed from the petri-dish so that 5.5 ml remained. The petri-dish is placed on the stage of a Nanoscope Dimension (Digital Instruments Inc.) AFM. An oxide-sharpened silicon nitride tip is used. The cantilever, a 120-μm-high isosceles triangle, has a spring constant of 0.06 Nm^{-1}. The microscope is operated in constant-force contact mode, and both height and deflection images are recorded. Surfaces of lysozyme crystals are very soft. In order to reduce tip-induced damage of the surface, the feedback controls are set to react quickly. Slow response runs the tip into the surface of the crystal, wearing out a square pattern.

Observations were carried out at room temperature, which can fluctuate. In our case we had a spread of 2°C during a single day of measurements and a range from 20.5^{o}C up to 24.5^{o}C for all experiments. During the AFM observations samples of solution of 100 μl were removed from the petri-dish at half hour intervals. From these samples the lysozyme concentration was determined by UV absorption measurements at 281.5 nm (absorption coefficient: 2.64 l g^{-1} cm^{-1} [12]). Temperature and concentration are necessary parameters to determine the driving force of crystal growth $\frac{\Delta\mu}{kT}$, which is given by

$$\frac{\Delta\mu}{kT} = \ln\frac{fc}{f_{eq}c_{eq}} \ , \qquad\qquad (2.1)$$

where k is Boltzmann's constant, T is the temperature, f and f_{eq} are activity coefficients, which we take as independent of concentration, and c and c_{eq} are the actual and equilibrium lysozyme concentrations, respectively, at a given temperature. To change the driving force $\frac{\Delta\mu}{kT}$ during AFM measurements, part of the solution was replaced with a more dilute solution of lysozyme.

2.3   Results and discussion

2.3.1   Morphology

Figure 2.1a shows a typical example of the triclinic lysozyme crystals grown in our laboratory for AFM measurements. From X-ray diffraction data we obtained the following cell parameters for the triclinic unit cell with space group P_1: a=27.18 Å, b=31.88 Å, c=34.21 Å, α=88.67^o, β=108.42^o and γ=111.98^o. These values are very close to the unit cell parameters reported in the literature [11] and confirm the identity of the triclinic pseudo-polymorph. Using angular measurements of crystals viewed in the optical microscope as well as single crystal X-ray diffraction measurements we indexed the crystal faces of our lysozyme crystals. The crystals were usually oriented in the petri-dish with either their (001) or (00$\bar{1}$) face upward*. Besides the (00±1), (0±10) and (±100) faces, which were always observed, in many cases we also encountered (1$\bar{1}$0) and ($\bar{1}$10).

To compare experiment with theory, the crystal shape was calculated by using the cell parameters and the computer program Facelift [13]. This program is based on the Hartman-Perdok theory [14], which relates crystal morphology to internal structure using bond energies between growth units. We start with finding the connected nets in the triclinic lysozyme structure. As a lysozyme molecule has many bonds of various strengths with each neighbouring molecule, we used the macrobond energies as derived by Matsuura and Chernov [15] to sum these. These bonds are used in Facelift to identify the connected nets and to calculate the vacuum attachment energies belonging to them (table 2.1). From the attachment energies we find the growth form by assuming that the growth rate of each face is proportional to its attachment energy[14]. Experiments and calculations show good agreement: both show the (±100), (0 ± 10), (00 ± 1), (1$\bar{1}$0) and ($\bar{1}$10) faces to be present in the morphology (figure 2.1b). The distance between the opposite (001) and (00$\bar{1}$) faces of our crystals is smaller than in the calculated morphology, because growth

---

*As the absolute configuration of the non-centrosymmetric crystal structure is not known, we are not able to distinguish between the faces (hkl) and ($\bar{h}\bar{k}\bar{l}$).
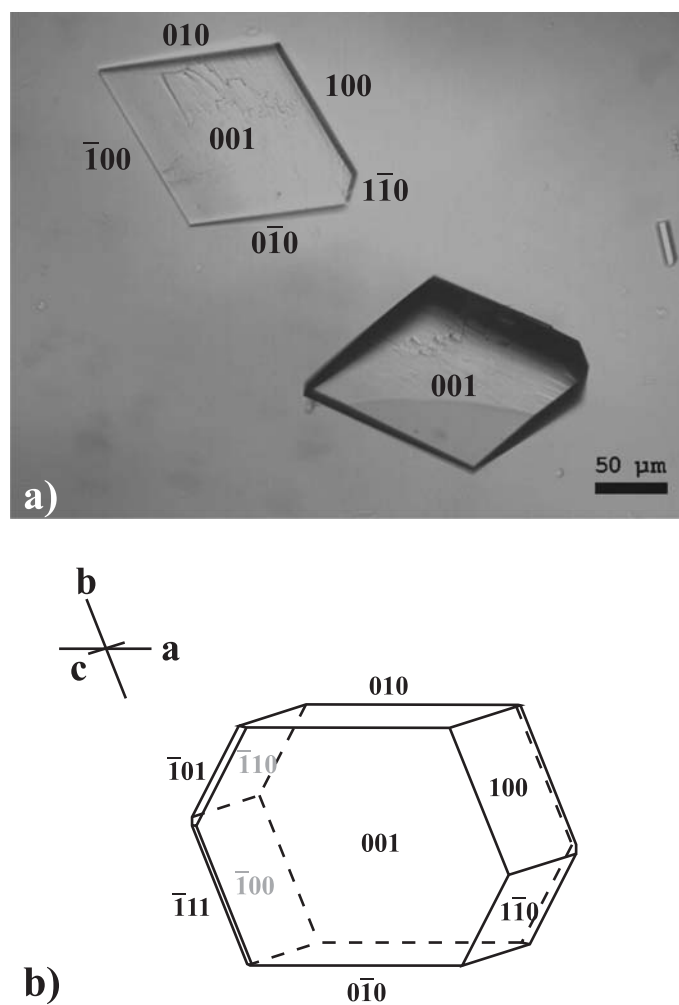
Figure 2.1: a) Optical view of triclinic hen egg-white lysozyme crystals, obtained in a 0.2 M NaNO$_3$, 50 mM acetate buffer solution as described in section 2.2. b) Morphology of triclinic lysozyme as calculated by Facelift. This is *not* a 3D representation, but a projection of the morphology on the *ab*-plane.

Table 2.1: Attachment energies in vacuum and interplanar distances for the connected nets of triclinic HEWL crystals on the basis of macrobonds.

Connected net (F-face)	$E_{Att.}$ (kJ/mol)	d_{hkl} (nm)
001	-382	3.23
010	-418	2.95
100	-464	2.39
$\bar{1}$10	-536	2.35
10$\bar{1}$	-706	2.33
1$\bar{1}\bar{1}$	-712	2.17

downwards is stopped by the glass bottom of the cell or petri-dish. $(1\bar{1}1)/(\bar{1}1\bar{1})$ and $(\bar{1}01)/(10\bar{1})$ faces are not found in our experiments. These faces are very small, and it might be difficult to reveal them by optical microscopy due to projection effects. We conclude that the macrobond concept introduced by Matsuura [15] is a good approximation for calculations on triclinic lysozyme.

2.3.2 Surface structure

AFM measurements on the (001) and $(00\bar{1})$ faces of triclinic lysozyme show various surface phenomena. Step sources were observed in the form of single and multiple growth spirals (figure 2.2a). We also found incorporation of sedimented particles (figure 2.2b). In a few cases we observed tip-induced 2D nucleation. Also 3D islands were observed. The step patterns often showed bunching and impurity pinning. The outcrops of both screw and edge dislocations at the surface are characterised by hollow cores. No differences in surface morphology were found on the opposite (001) and $(00\bar{1})$ faces. Therefore in the rest of this paper both faces are indexed as (001).
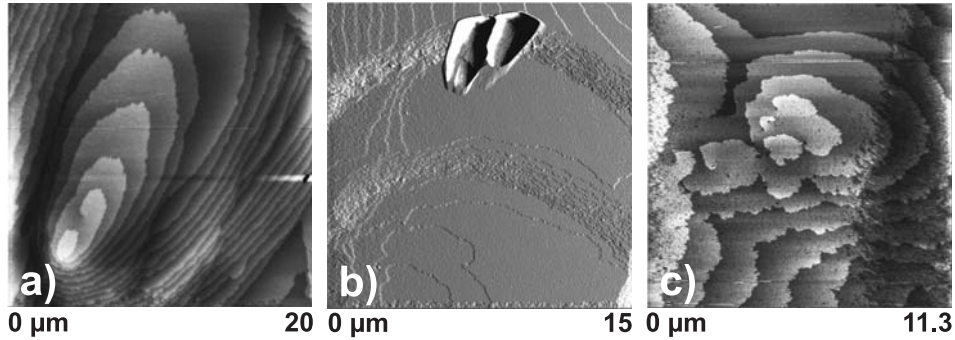
Figure 2.2: *In-situ* AFM images of growth patterns on the (001) face of triclinic lysozyme crystals. (a) Height image showing a double spiral. (b) Deflection image of a sedimented particle being incorporated into the crystal. (c) Height image of an array of dislocations. On the left and right side of image (c), scan-induced damage to the surface is visible.

Spirals and other step sources

A variety of growth spirals was found: single spirals, double spirals, closed loop steps originating from dislocation pairs of opposite sign, and dislocation arrays (see figure 2.2c). The step height of these spirals was always 3.2 ± 0.2 nm, matching the interplanar distance, d_{001}, of 3.23 nm. This height also corresponds to approximately the diameter of one lysozyme molecule.

Individual or groups of dislocations are the sources of the spirals. The component of the Burgers vector perpendicular to the surface, $b_\perp$, is equivalent to d_{001}. All spirals found are rounded, regardless of supersaturation, and polygonal spirals were not observed. The spiral shapes were found to be highly anisotropic (see figure 2.3a), appearing elliptical with the long axis parallel to the [010] direction. Besides the anisotropy between the $<010>$ and the $<100>$ directions, a strong anisotropy exists between the [010] and the [0$\bar{1}$0] direction. This indicates a large difference in step velocity for these opposite directions. Entire triclinic lysozyme crystals also show polar growth along $<010>$, as we concluded from in-situ optical microscopic observations.

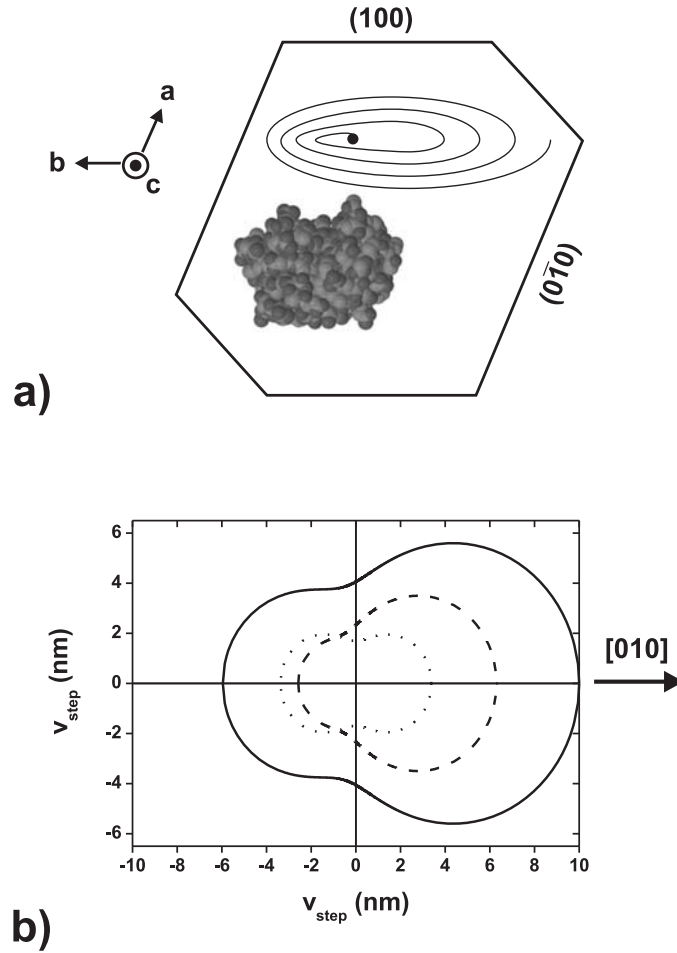While spirals are the main source of steps on the (001) surface of triclinic

Figure 2.3: Morphology of the anisotropic spirals on (001) lysozyme. a) Orientation of spirals with respect to the crystal habit. A lysozyme molecule is drawn to show its orientation with respect to crystal habit. b) Kinetic Wulff plot showing step velocity versus step orientation for spirals on the (001) surface at $\frac{\Delta\mu}{kT} = 0.4$ (dashed line) and $\frac{\Delta\mu}{kT} = 1.2$ (solid line). Spirals are approximated by ellipses to simplify the reconstruction. The dotted line shows the Wulff plot in case the growth centre would lie at the centre of the ellipse.

HEWL, other sources do occur. Step sources in the form of 3D islands were observed (see figure 2.4). These islands are likely to originate from sedimented particles, as reported by e.g. [[16, 17]], which may originate from the solution-air interface where the local supersaturation is increased due to evaporation. The islands expand as step bunches of typically 40-80 steps high. The accumulated steps propagate at a slightly slower rate than the mono-molecular steps of the spirals. The 3D islands show the same anisotropy as the spirals.

In a few cases we observed 2D nucleation of islands. Taking into account their position at the edges of the AFM scan range, these nuclei are likely a result of tip-surface interaction. Two-dimensional nucleation does not play a role as a step source for any of the applied supersaturations in this study.

Steps

The step speed is anisotropic, as is clear from the shape of the spirals. The shape of the spirals at large distance from the growth centres is determined by the anisotropy in step velocity. Using a two-dimensional inverse kinetic Wulff construction [18] it is possible to determine the step speed as a function of the orientation from the shape of the spirals (see appendix). Figure 2.3b shows the Wulff plots obtained in this way for low and high $\frac{\Delta\mu}{kT}$. The step velocity is higher for the high $\frac{\Delta\mu}{kT}$, but the polar velocity plots are similar in shape, thus the anisotropy in step propagation changes little with supersaturation.

Step speeds for the slowest step directions were determined from series of scans at various supersaturations. Figure 2.5 shows the results as function of HEWL concentration and of driving force $\frac{\Delta\mu}{kT}$. We find the step speed to be linear in its concentration dependence:

$$v_{step} = \beta \frac{c - c_{eq}}{c_{eq}} \ ,\qquad (2.2)$$

in which c_{eq} is 0.4 mg/ml and β is 2.9 nm/s. The equilibrium concentration was verified by additional experiments in which the occurrence of growth or dissolution of seeded triclinic HEWL crystals was examined in solutions of different concentrations around c_{eq}. The linear dependence of the step velocity
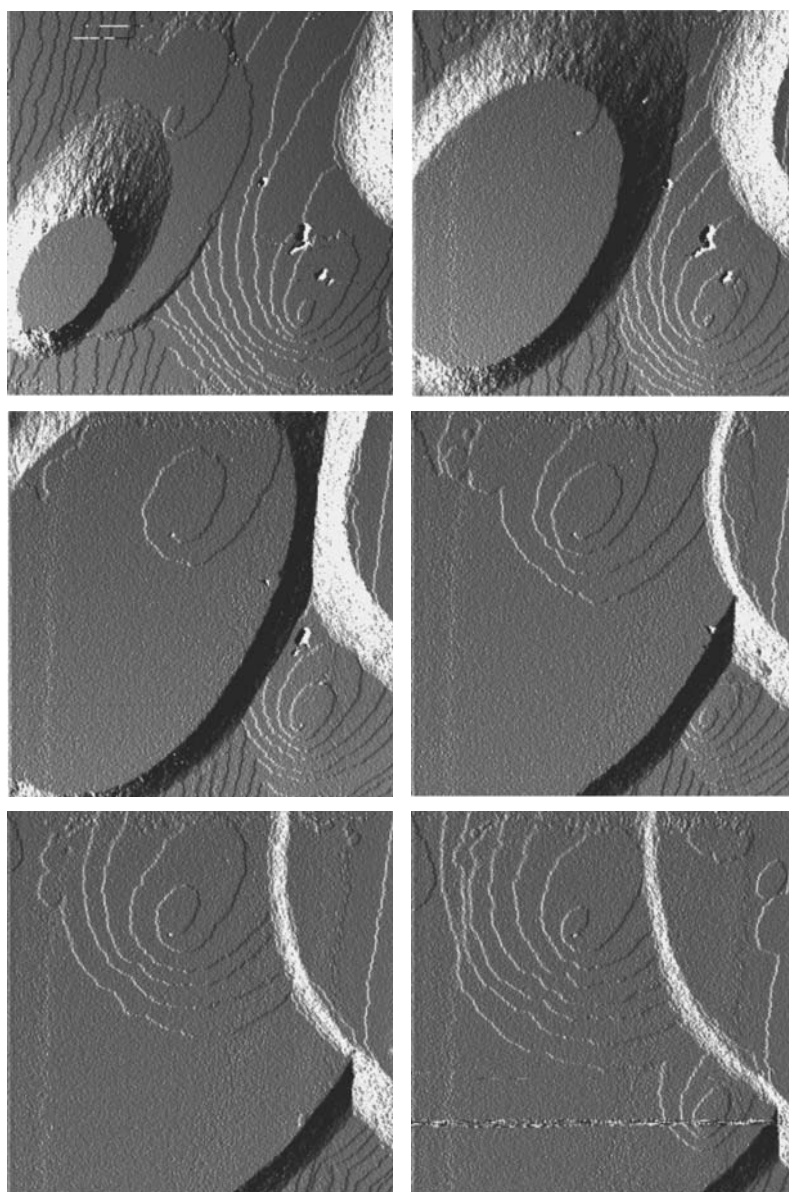
Figure 2.4: Series of *in-situ* AFM deflection images of a 20 μm x 20 μm surface area showing the evolution of 3D islands on the (001) face of triclinic lysozyme. The pictures are recorded at a 8.5 minute interval. Spirals and hollow cores are overgrown by the islands, but reappear on top.
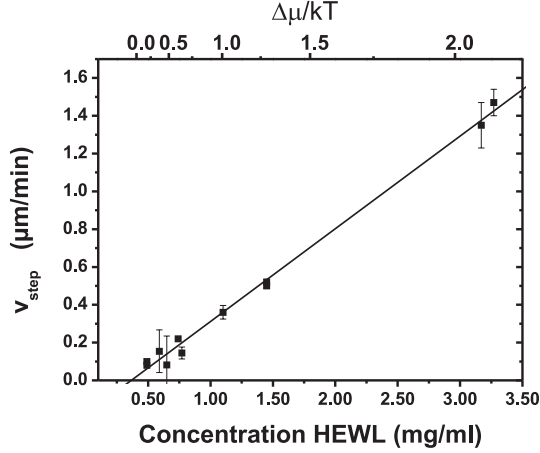
Figure 2.5: Step velocity as a function of HEWL concentration and driving force. The step velocities are averaged values for those directions that correspond with the "slowest" 180° segment of the kinetic Wulff plot. The average temperature is 295 K.

complies with the linear law of Wilson-Frenkel [19, 20]:

$$
\begin{aligned}
v_{step} &\propto J_0 \left(e^{\Delta\mu/kT} - 1 \right) \\
&\approx J_0 \frac{c - c_{eq}}{c_{eq}} \ ,
\end{aligned}
\tag{2.3}
$$

where equation (2.1) was used to rewrite the exponential.

All spirals observed were rounded, even for the driving force approaching zero. This indicates a high kink density of the steps and thus low kink energies ϕ_k. Another possible cause of the roundness of the spirals is impurity pinning. As the step speed is proportional to the supersaturation σ, this influence must be small.

Impurity pinning has been observed on protein crystals [21] before, including tetragonal lysozyme [22]. Although in our experiments the influence of impurity pinning on step propagation is small, serrated step patterns as shown in figure 2.6 provide evidence for its presence. This conclusion is supported
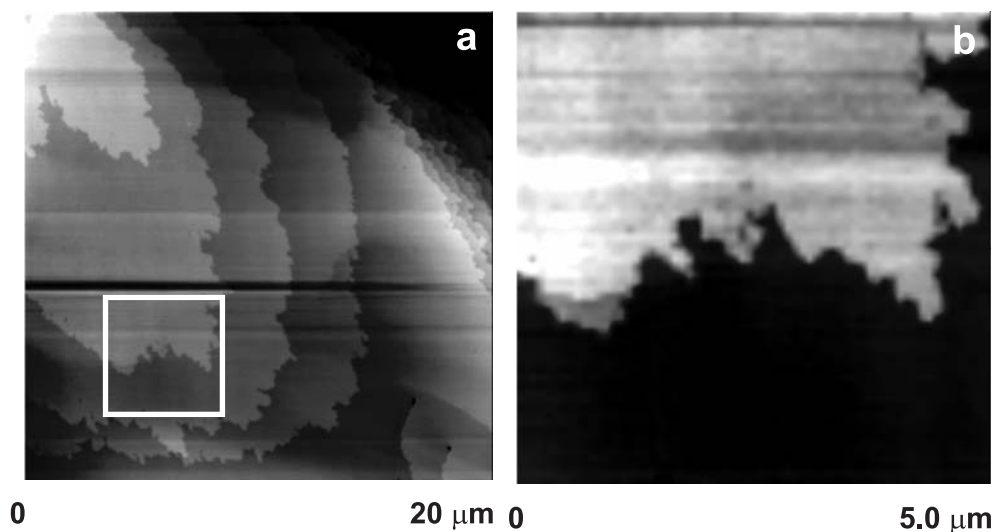
Figure 2.6: Impurity pinning of steps on the (001) face of triclinic lysozyme. a) AFM scan giving an overview of the serrated step patterns. In some areas, the shape of subsequent steps is roughly the same, which confirms impurity pinning. b) Detail, showing the part outlined by the square in a). The two deep 'fjords' indicate local blocking of steps by impurities.

by the fact that the perturbed patterns are often repetitive for subsequent steps. Steps are blocked completely by impurities if the distance d between adjacent impurities is smaller than twice the radius of the critical nucleus size, i.e. $d < 2\,r_c$. The critical radius, r_c, depends on the edge free energy γ and the driving force. Thus, also the critical distance d_{crit} depends on γ and $\Delta\mu$:

$$d_{crit} = \frac{2\gamma\Omega}{\Delta\mu} \; , \tag{2.4}$$

in which Ω is the volume of one growth unit (25.9 nm^3 for triclinic lysozyme). As the edge free energy for triclinic lysozyme crystals is not available in literature, we use that of tetragonal lysozyme. For tetragonal lysozyme literature reports values[†] in the order of 1 mJ/m^2 [7, 23–25]. To calculate an upper limit for the critical distance d_{crit}, we use the largest value of γ from literature

[†]In the protein literature edge free energy is often expressed as a measure of energy per

and the smallest value of $\Delta\mu$ from our experiments. We find $d_{critical} <$75 nm. Locally, blocking can occur by inhomogeneously distributed groups of closely separated impurities, with the steps flowing around these groups. Such a mechanism is suggested by the presence of deep "fjords" (figure 2.6b). However, on average, the distance between pinning points is larger than d_{crit}, the smallest observed distance being 180±10 nm, and impurity blocking is not expected to occur. Moreover, if impurity adsorption had a strong blocking effect, step bunches would move faster than individual steps [26]. We observed the opposite, which is in compliance with the limited role of impurities. To get an idea of the molecular weight of the impurities in the source material, we performed Matrix Assisted Laser Decoupling/Ionising Time-of-Flight (MALDI-TOF) measurements on our HEWL material. The impurities found by this method were of low molecular weight (< 5 kDa).

Hollow cores

Similar to other types of protein crystals [16, 27, 28], the outcrops of dislocations ending at the (001) surface of the triclinic lysozyme crystals are marked by hollow cores. The hollow cores remain present even when step bunches pass over them (see figure 2.4). Two types of hollow cores were observed. The first type emits steps and it produces either spirals (figure 2.4) or extra steps in step trains (figure 2.7). Steps emitted from hollow cores of this type all have a height of d_{001}, indicating screw dislocations with a Burgers vector b=[001]. As for a given supersaturation the hollow core radii of this type are all the same, we do not expect an extra edge component [100] or [010] for the dislocations, because in that case a part of the hollow cores would be wider.

The second type of hollow core does not emit steps (see figure 2.7). Here only edge dislocations are involved. As the hollow core radii have practically the same size as that of screw dislocations, the Burgers vector must be comparable in length. Edge dislocations have a Burgers vector of either [100] or [010], which is close to the Burgers vector length $|[001]|$ of a screw disloca-

---

molecule. Conversion from "per molecule" to "per square meter" depends on the choice of surface area per molecule.
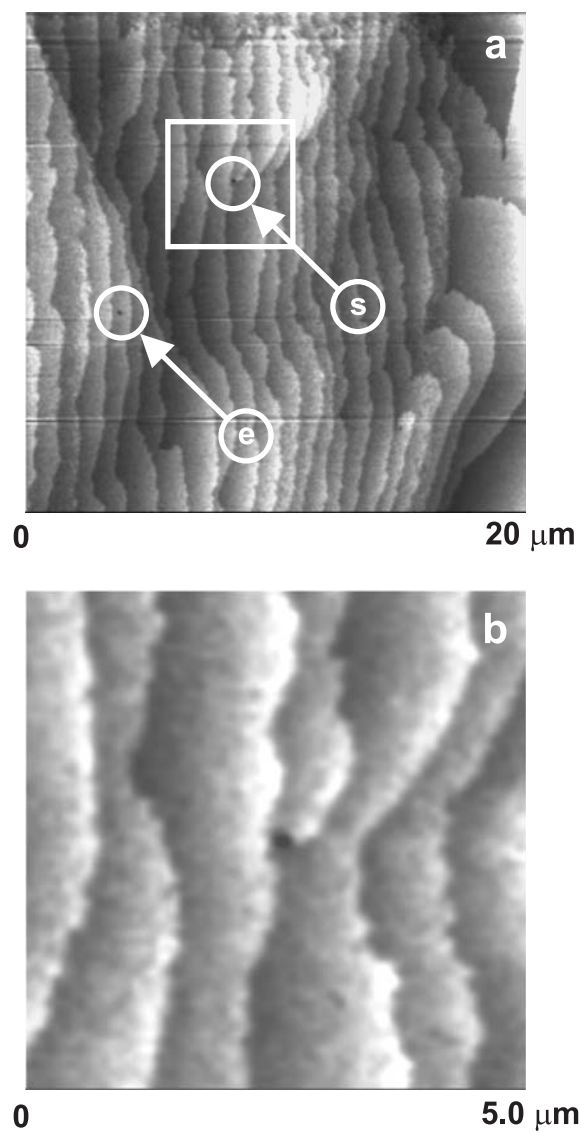
Figure 2.7: a) AFM height image showing hollow core outcrops on the (001) surface of triclinic lysozyme. Arrows indicate a screw (s) and an edge (e) dislocation. b) Detail showing the hollow core in the part outlined by the square in figure a).
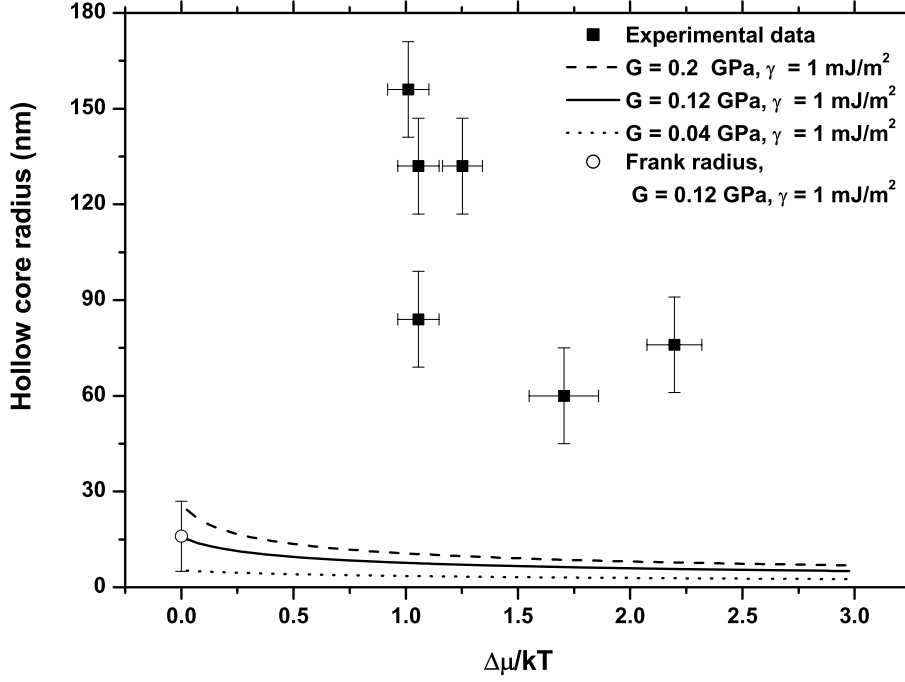
Figure 2.8: Hollow core radius versus driving force. Squares indicate experimental data. The circle indicates the (calculated) Frank radius for $\gamma = 1\ mJ/m^2$ and $G = 0.12\ GPa$. The lines indicate calculated hollow core radii as a function of driving force $\frac{\Delta\mu}{kT}$ for $\gamma = 1\ mJ/m^2$ and various shear moduli G. Experimental data are an order of magnitude larger than theoretical values.

tion. Thus, dislocations ending on the (001) surface of triclinic lysozyme have Burgers vectors [001], [100] or [010].

For various driving forces, radii of hollow cores associated with screw dislocations were determined by recording cross sections through the hollow cores in the AFM height images (figure 2.8). The theoretically expected hollow core size follows from thermodynamic models [29–31] as well as from the analysis of an isotropic growth spiral [32], both considering the stress field around its dislocation:

$$r_{hc} = -\frac{\gamma\,\Omega}{2\,\Delta\mu}\left(1 - \sqrt{1 + 4\frac{G\,b^2\,\Delta\mu}{8\pi^2\,\gamma^2\,\Omega}}\,\right)\ . \qquad (2.5)$$

In this equation, r_{hc} is the hollow core radius, b the length of the Burgers vector and G the shear modulus. Using literature data on the Young's modulus for triclinic lysozyme crystals [33] and a Poisson's ratio of 0.25, the shear modulus was calculated to be 0.12±0.08 GPa. The calculated hollow core radius for an edge free energy of 1 mJ/m^2 versus driving force is indicated by the lines in figure 2.8. The open circle indicates the Frank radius [29],

$$ r_f = \frac{G\,b^2}{8\,\pi^2\,\gamma} \; , \tag{2.6} $$

using the same parameter values. This radius corresponds with the theoretical size of the hollow core at equilibrium. The measured core radius decreases with increasing driving force, as is expected from theory. Data, however, show that the observed hollow core radii are one order of magnitude larger than theory. Great care should be taken in interpreting measured hollow core sizes. It is energetically unfavourable for a hollow core to simply end at the surface. At the surface, a trumpet-shaped hollow core outcrop develops as described by Frank [29] and Srolovitz and Safran [34] for equilibrium. Combined TEM and AFM measurements on GaN confirm the existence of such craters [35]. Due to the AFM tip radius of about 20 nm the crater region is imaged, but the actual hollow core is not. It cannot descent down a hollow core of comparable radius more than approximately 5 nm. The combination of a crater-like outcrop and limitations due to the AFM tip size results in measuring a wider and more shallow pattern than the actual hollow core[35]. Liu *et al.* [36] modelled the shape of the crater region at equilibrium and at $\frac{\Delta\mu}{kT} = 0.2$ using Monte Carlo simulations. These indicate a steeper crater region for $\frac{\Delta\mu}{kT} > 0$. Although we did not measure the actual core size, the supersaturation dependence of the core radius is expected to be reflected in the measured crater radii.

2.4 Step energetics and kinetics

2.4.1 Energetics

As mentioned above, the fact that the steps are rounded implies a low kink energy and thus a high kink density. For the (001) face of a Kossel crystal the

transition between rounded and polygonised spirals occurs for a kink energy $\phi_k/kT \approx 1.5$[37], which corresponds with a kink density of $n_k \approx 0.37$ [38]. So for (001) triclinic lysozyme $\phi_k/kT \leq 1.5$, if we assume a similar behaviour of the connected net in the d_{001} slice. On the other hand, the edge free energy must be relatively high, as no 2D nuclei were observed. This apparent contradiction can be explained by looking at the connected net in the d_{001} slice, as shown in figure 2.9 for a step parallel to [010]. For the other steps the situation is similar. For this simple crystal graph the kink and edge energy are proportional to $\frac{1}{2}E_D$ and $\frac{1}{2}(E_C + E_A)$ respectively. Since the macrobond energies E_A, E_C and E_D do not differ too much [15], one can state that the edge energy is roughly twice the kink energy. For the Kossel crystal the edge energy is lower, being equal to the kink energy.
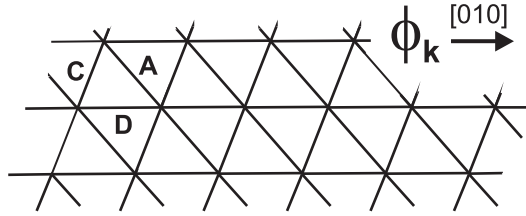

Figure 2.9: Connected net in the d_{001} slice of triclinic HEWL showing a step parallel to [010]. Bond notation is according to Matsuura and Chernov [15]. A kink is indicated by ϕ_k.

An alternative way to make an estimate of ϕ_k/kT using the equivalent wetting assumption[14]:

$$\frac{\phi_k}{kT} = \frac{1}{2}\frac{E_D}{E_{cryst}} \times \frac{\Delta H_{diss}}{RT} \ . \tag{2.7}$$

This gives ϕ_k/kT=3.7, which is too high. From this value it follows that we have "more than equivalent wetting" [39], i.e. a situation in which the solvent interacts stronger with the crystal surface than with dissolved protein molecules.

A lower limit for ϕ/kT can be obtained from the fact that the surface was never kinetically roughened, even for the highest $\frac{\Delta\mu}{kT} = 2$. Thus, the critical

nucleus size was always larger than one growth unit. This sets a lower limit
to the edge energy per molecule γ_m of

$$\frac{\gamma_m}{kT} > \frac{1}{2}\frac{\Delta\mu}{kT} \ , \tag{2.8}$$

which follows from the expression for the critical nucleus $r^* = \gamma\Omega/\Delta\mu$ with
the edge energy γ *per square meter* . Thus, $\gamma_m/kT \approx 2\phi/kT$ is larger than 1.
As for (001) lysozyme $\phi_k \approx \phi$, it follows from the above that the edge energy
must be confined between

$$1 < \frac{\gamma_m}{kT} < 3 \ .$$

If we consider an edge free energy of tetragonal lysozyme of 1.2 mJ/m^2 [24] and
an effective surface of 3 by 3 nm (i.e. approximately one side of the molecule),
we find γ_m/kT is 1.3 for this crystal form. This edge free energy is within
the range we find for triclinic lysozyme. At a driving force of 0.5 tetragonal
lysozyme grows by 2D nucleation[7], whereas for triclinic HEWL 2D nucleation
is absent up to a driving force of at least 2. Thus, the edge free energy of the
triclinic form will be higher than $1.3kT$.

For isotropic spirals, the step spacing far away from the spiral centre is
related to the critical radius by [30]

$$\Delta r^\infty = 19r_c \ . \tag{2.9}$$

At $\frac{\Delta\mu}{kT}$ =1 the critical radius is between 3 to 9 nm for $1 < \frac{\gamma_m}{kT} < 3$. Thus, the
step spacing of the spiral arms should be 60-180 nm for this supersaturation.
However, experiment shows step spacings varying from 1 up to 5 μm, which
is one order of magnitude larger. This discrepancy is explained by the fact
that the stress field of the dislocation associated with the hollow core slows
down the rotation speed of the spiral [40]. For constant step speed this results
in a larger step spacing. A simple expression for the step spacing of a spiral
emerging from a central obstacle with perimeter length P has been put forward
by De Yoreo *et al.* [40]:

$$\lambda = 19\,r_c + P \ . \tag{2.10}$$

For a hollow core the length of the perimeter is $P = 2\pi r_{hc}$, in which the crater region is included in r_{hc}. Using measured values of $r_{hc} \approx 150$ nm we now come to step spacings of about 1 μm, which is the right order of magnitude.

2.4.2 Kinetics

The propagation velocity of a step v_{step} is determined by the kink length w, the kink density (number of kinks per step site) n_k, and the effective addition frequency of growth units into a kink position, v_{eff} [38, 41, 42]:

$$v_{step} = n_k \cdot w \cdot \nu_{eff} \ . \tag{2.11}$$

The effective addition frequency is the difference between the addition frequency and the removal frequency of growth units to and from a kink site: $\nu_{eff} = \nu_{add} - \nu_{rem}$. The addition frequency is given by:

$$\begin{aligned} \nu_{add} &= \chi \, S \, \nu_o \\ &= \chi_{eq} \, \exp^{\Delta\mu/kT} \, S \, \nu_o \ , \end{aligned} \tag{2.12}$$

in which χ is the volume fraction of growth units (instead of concentration, as the protein growth units are much larger than the solvent molecules). ν_0 is the number of times per second a growth unit adjacent to a kink attempts to stick to this position. S is the sticking fraction, i.e. the chance that such an attempt is successful. The removal frequency is assumed to be independent of supersaturation.

At equilibrium ($\Delta\mu = 0$), the removal frequency is equal to the addition frequency:

$$\nu_{rem} = \chi_{eq} \, \exp^{0/kT} \, S \, \nu_o \ . \tag{2.13}$$

Thus, the effective addition frequency becomes

$$\begin{aligned} \nu_{eff} &= \chi_{eq} \, S \, \nu_o \left[\exp^{\Delta\mu/kT} - 1 \right] \tag{2.14} \\ &= \chi_{eq} \, S \, \nu_o \, \sigma \ , \tag{2.15} \end{aligned}$$

in which σ is the relative supersaturation defined by $\frac{\chi - \chi_{eq}}{\chi_{eq}} \cong \frac{c - c_{eq}}{c_{eq}}$.

The time for a lysozyme molecule to displace over a distance $d \approx (\bar{d}^2)^{1/2}$ in its solution is given by $t = \frac{\bar{d}^2}{6D}$, with D the diffusion constant [43]. Since addition to a kink site proceeds by a "jump" downwards over the step height, h, and movement upwards and in the horizontal directions does not play a role, it follows that

$$\nu_o \cong (6t)^{-1} \cong \frac{D}{h^2} \; . \tag{2.16}$$

Substituting 2.15 and 2.16 into 2.11 we find for the step speed

$$v_{step} = n_k \, w \, \chi_{eq} \, S \, \frac{D}{h^2} \, \sigma \; . \tag{2.17}$$

So, the sticking fraction S becomes

$$S \;\; = \;\; \frac{v_{step} \, h^2}{n_k \, w \, \chi_{eq} \, D \, \sigma} \tag{2.18}$$

$$= \;\; \frac{\beta \, h^2}{n_k \, w \, \chi_{eq} \, D} \; , \tag{2.19}$$

in which β is the kinetic coefficient. β is 2.9 nm/s as determined by experiment (see section 2.3.2). The kink density n_k is about 0.5, as the steps in our experiments are rounded. By approximating the HEWL molecule by a cube of 3 by 3 nm we take the step height h and kink length w to be 3 nm. The equilibrium volume fraction of lysozyme χ_{eq} is approximately 4×10^{-4}. From literature we take an averaged value of the diffusion coefficient for lysozyme in a 0.05 M NaAc buffer and NaCl as precipitating agent, which is 1.2×10^{-10} $m^2 \, s^{-1}$ [44, 45]. Thus, we find a sticking fraction S of 4×10^{-4} for triclinic lysozyme. For [100] steps on (010) orthorhombic lysozyme the sticking fraction was found to be in the order of 10^{-6} [9]. The kink sites of the orthorhombic crystals are made up of four molecules, which results in four different sticking fractions for the individual molecules. Some of the additions are less favourable than others, leading to a lower average S than in the case of our triclinic crystals with only one molecule per kink site. Also, orthorhombic lysozyme is grown from a chloride solution in stead of a nitrate solution. Kink kinetics and pre-kink orientation requirements may therefore differ significantly.

2.5   Conclusions

The observed morphology of triclinic HEWL crystals grown for *in-situ* AFM measurements on the (001) face is in agreement with the morphology derived from the connected net analysis using the macrobond concept by Matsuura and Chernov[15]. AFM images show rounded steps, single and multiple growth spirals with large anisotropy, hollow cores and step bunching.

The main step sources are the growth spirals, although 3D nucleation was also observed. Step patterns indicate the occurrence of impurity pinning. However, steps are not blocked completely by the impurities. Both screw and edge dislocations are marked by hollow core outcrops at the surface. But the radii of the hollow cores are one order of magnitude larger than theoretical values, which is explained by their trumpet shaped emergence at the surface. The velocity of the steps is proportional to the relative supersaturation. From morphology and the experimentally determined kinetic coefficient we find a sticking fraction $S=4\times10^{-4}$ for a protein molecule to become attached to a kink site, which is significantly different compared to the sticking fraction for orthorhombic lysozyme. From the rounded shape of the spirals and the absence of 2D nucleation we conclude that the step free energy must be in the range $1.3< \gamma_m/kT <3$, which is comparable to values of tetragonal lysozyme.

Acknowledgements

Appendix A: Inverse Wulff construction applied to growth spirals

The inverse Wulff construction is used to obtain a polar plot of step velocity versus step orientation from spiral shapes imaged by AFM. In this an ellipse is used as an approximation of the more or less elliptically shaped growth spirals.

For an ellipse with the centre at (0,0) we can write the following expression:

$$\frac{x^2}{k^2} + \frac{y^2}{(k-1)^2} = p^2 \ , \tag{A.1}$$

in which, k and p are constants defining the ellipse. Equation A.1 can be rewritten as a function $f(x)$

$$f(x) = \pm(k-1)\sqrt{p^2 - \frac{x^2}{k^2}} \ , \tag{A.2}$$

in which the $\pm$ indicates the top and bottom sides of the ellipse. The first step in performing the inverse Wulff construction is to find the tangent for every point of the ellipse. Then, we draw a line perpendicular to the tangent. This line should run through the so-called growth centre, which is the dislocation outcrop for a spiral (see figure A.1). The growth centre can be any point within the ellipse.
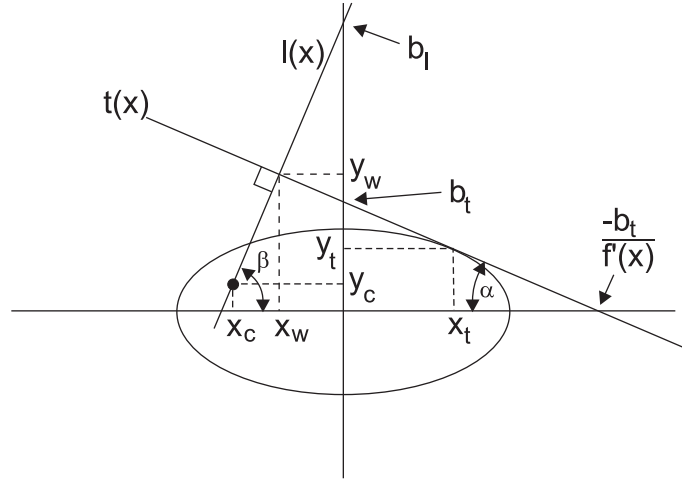

Figure A.1: Principle of the inverse Wulff construction starting from an elliptical spiral shape.

Thus, the first step is to find the tangent in every point of the ellipse. The derivative of $f(x)$

$$f'(x) = \pm\frac{(1-k)}{k^2}\frac{x}{\sqrt{p^2 - \frac{x^2}{k^2}}} \ , \tag{A.3}$$

gives the direction of the tangent for all points on the ellipse. As one can see, for $x = pk$ this results in a division by zero, i.e. a vertical line. The tangent $t(x)$ can be written as

$$t(x) = f'(x_t)\, x + b_t \ , \tag{A.4}$$

in which $f'(x_t)$ is the derivative of the ellipse, and thus the slope of the tangent line, in point x_t of the ellipse, and b_t is the intersection of the tangent with the vertical y-axis. In the point where the tangent touches the ellipse, at (x_t, y_t) (see figure A.1), we find that $f(x_t) = t(x_t)$. We can use this fact to find a value for b_t:

$$b_t = f(x_t) - f'(x_t)\, x_t \ . \tag{A.5}$$

Next step is to define the line perpendicular to $t(x)$ that passes through the growth centre (x_c, y_c). For this perpendicular line $l(x)$ we can derive:

$$\begin{aligned} l(x) &= a_l x + b_l \\ &= x \tan \beta + b_l \ , \end{aligned} \tag{A.6}$$

in which $\beta = (\frac{1}{2}\pi - \alpha)$ as defined in figure A.1. In the resulting equation b_l is unknown. Since $\beta = \frac{1}{2}\pi + \arctan[f'(x_t)]$ we can write for b_l

$$\begin{aligned} b_l &= y_c - x_c \tan \beta \tag{A.7} \\ &= y_c - x_c \tan\left(\frac{1}{2}\pi + \arctan\left(f'(x_t)\right)\right) \ . \tag{A.8} \end{aligned}$$

Now we can find the intersection point of the tangent and the perpendicular line, which is the point (X_W, Y_W) on the Wulff plot corresponding to the point (x_t, y_t) on the ellipse. This is the point where $t(X_W) = l(X_W)$:

$$\begin{aligned} f'(x_t)\, X_W + b_t &= X_W \tan \beta + b_l \tag{A.9} \\ (f'(x_t) - \tan \beta) X_W &= b_l - b_t \tag{A.10} \\ X_W &= \frac{(b_l - b_t)}{f'(x_t) - \tan \beta} \ . \tag{A.11} \end{aligned}$$

By substituting X_W in either equation A.4 or A.6 we find Y_W

$$Y_W = \frac{(b_l - b_t)\tan\beta}{f'(x_t) - \tan\beta} + b_l \ .$$ (A.12)

The complete set of points (X_W, Y_W) represents the polar Wulff plot, which relates step velocity to step orientation.

References

[1] McPherson, A. *Crystallization of Biological Macromolecules;* Cold Spring Harbor Laboratory Press: New York, 1999.

[2] Ries-Kautt, M.; Ducruix, A. F. *J. Biol. Chem.* **1989,** *264,* 745-748.

[3] Vaney, M.; Broutin, I.; Retailleau, P.; Douangamath, A.; Lafont, S.; Hamiaux, C.; Prange, T.; Ducruix, A.; Ries-Kautt, M. *Acta Crystallogr., Sect. D* **2001,** *57,* 9229-9240.

[4] Steinrauf, L. *Acta Crystallogr.* **1959,** *12,* 77-79.

[5] Legrand, L.; Ries-Kautt, M.; Robert, M. *Acta Crystallogr., Sect. D* **2002,** *58*, 1564-1567.

[6] Durbin, S.; Carlson, W. *J. Cryst. Growth* **1992,** *122,* 71-79.

[7] Gorti, S.; Forsythe, E.; Pusey, M. *Cryst. Growth Des.* **2005,** *5,* 473-482.

[8] Rashkovich, L.; Gvozdev, N.; Sil'nikova, M.; Chernov, A. *Crystallogr. Rep.* **2002,** *47,* 859-866.

[9] Chernov, A.; Rashkovich, L.; Yaminski, I.; Gvozdev, N. *J. Phys.: Condens. Matter* **1999,** *11,* 9969-9984.

[10] Kossel, W. *Angew. Chem.* **1952,** *64,* 276.

[11] Walsh, M.; Schneider, T.; Sieker, L.; Dauter, Z.; Lamzin, V.; Wilson, K. *Acta Crystallogr., Sect. D* **1998,** *54,* 522-546.

[12] Aune, K.; Tanford, C. *Biochemistry* **1969,** *8,* 4579-4585.

[13] Boerrigter, S.; Grimbergen, R.; Meekes, H. 2001 FACELIFT-2.50, a program for connected net analysis, Dept. of Solid State Chemistry, Radboud University of Nijmegen; email: H.Meekes@science.ru.nl.

[14] Bennema, P. . In *Handbook of Crystal Growth*, Vol. 1a; North-Holland: 1993; Chapter 7.

[15] Matsuura, Y.; Chernov, A. *Acta Crystallogr., Sect. D* **2003,** *59,* 1347-1356.

[16] Kuznetsov, Y.; A.J. Malkin, A. M. *J. Cryst. Growth* **1999,** *196,* 489-502.

[17] Waizumi, K.; Plomp, M.; van Enckevort, W. *Colloids Surf., B* **2003,** *1-2,* 73-86.

[18] Wulff, G. *Z. Kristallogr. Miner.* **1901,** *34,* 449-530.

[19] Wilson, H. *Philos. Mag.* **1900,** *50,* 238.

[20] Frenkel, J. *Phys. Z. Sowjetunion* **1933,** *1,* 498.

[21] Plomp, M.; A. McPherson, A. M. *Proteins: Struct., Funct., Genet.* **2003,** *50,* 486-495.

[22] Nakada, T.; Sazaki, G.; Miyashita, S.; Durbin, S.; Komatsu, H. *J. Cryst. Growth* **1999,** *196,* 503-510.

[23] Durbin, S.; Feher, G. *J. Cryst. Growth* **1986,** *76,* 583-592.

[24] Chernov, A. *Phys. Rep.* **1997,** *288,* 61-75.

[25] Fiddis, R.; Longman, R.; Calvert, P. *J. Chem. Soc.* **1979,** *75,* 2753.

[26] Land, T.; Martin, T.; Potapenko, S.; Palmore, G.; Yoreo, J. D. *Nature* **1999,** *399,* 442-445.

[27] Land, T.; Malkin, A.; Kuznetsov, Y.; McPherson, A.; De Yoreo, J. *Phys. Rev. Lett.* **1995,** *75,* 2774-2777.

[28] Wang, S.; Li, G.; Xiang, Y.; Huang, R.; Zhang, Y.; Wang, D. *Acta Crystallogr., Sect. D* **2005,** *61,* 826-831.

[29] Frank, F. *Acta Crystallogr.* **1951,** *4,* 497-501.

[30] Cabrera, N.; Levine, M. *Philos. Mag.* **1956,** *1,* 450-458.

[31] van der Hoek, B.; van der Eerden, J.; Bennema, P. *J. Cryst. Growth* **1982,** *56,* 621-632.

[32] van der Hoek, B.; van der Eerden, J.; Bennema, P. *J. Cryst. Growth* **1982,** *56,* 108-124.

[33] Vekilov, P.; Chernov, A. *Solid State Physics* **2002,** *57,* 1-147.

[34] Srolovitz, D.; Safran, S. *Philos. Mag., Sect. A* **1985,** *52,* 793-800.

[35] Qian, W.; Rohrer, G.; Skowronski, M.; Doverspike, K.; Rowland, L.; Gaskill, D. *Appl. Phys. Lett.* **1995,** *67,* 2284-2286.

[36] Liu, G.; van der Eerden, J.; Bennema, P. *J. Cryst. Growth* **1982,** *58,* 152-162.

[37] van Enckevort, W. . In *Facets of 40 years of crystal growth. A tribute to Piet Bennema on the occasion of his retirement*; IMM department of Solid State Chemistry, Radboud University Nijmegen: 1997.

[38] Burton, W.; Cabrera, N.; Frank, F. *Philos. Trans. R. Soc. London, A* **1951,** *243,* 299-358.

[39] Liu, X.; Bennema, P. *J. Chem. Phys.* **1993,** *98,* 5863-5872.

[40] DeYoreo, J.; Land, T.; Rashkovich, L.; Onischenko, T.; Lee, J.; Monovskii, O.; Zaitseva, N. *J. Cryst. Growth* **1997,** *182,* 442-460.

[41] van der Eerden, J. . In *Handbook of Crystal Growth*, Vol. 1a; North-Holland: 1993; Chapter 5, page 307.

[42] Cuppen, H.; Meekes, H.; van Veenendaal, E.; van Enckevort, W.; Bennema, P.; Reedijk, M.; Arsic, J.; Vlieg, E. *Surf. Sci.* **2002,** *506,* 183-195.

[43] Moore, J.; Pearson, R. *Kinetics and mechanisms;* John Wiley & Sons: 3 ed.; 1981.

[44] Muschol, M.; Rosenberger, F. *J. Chem. Phys.* **1995,** *103,* 10424-10432.

[45] Kim, Y.; Myerson, A. *J. Cryst. Growth* **1994,** *143,* 79-85.